ACS Partner Journal

Journal of the American Society for Mass Spectrometry

pubs.acs.org/jasms

Research Article

Improving the Performance of a Cycloidal Coded-Aperture Miniature Mass Spectrometer

Raul Vyas, Tanouir Aloui, Kathleen Horvath, Philip J. Herr, Matthew P. Kirley, Charles B. Parker, Adam D. Keil, James B. Carlson, Justin Keogh, Roger P. Sperline, M. Bonner Denton, M. Luisa Sartorelli, Brian R. Stoner, Michael E. Gehm, Jeffrey T. Glass, and Jason J. Amsden*

Cite This: *J. Am. Soc. Mass Spectrom.* 2021, 32, 509−518

Read Online

ACCESS | Metrics & More | Article Recommendations | Supporting Information

ABSTRACT: Cycloidal sector mass analyzers have, in principle, perfect focusing due to perpendicularly oriented uniform electric and magnetic fields, making them ideal candidates for incorporation of spatially coded apertures. We have previously demonstrated a proof-of-concept cycloidal-coded aperture miniature mass spectrometer (C-CAMMS) instrument and achieved a greater than 10-fold increase in throughput without sacrificing resolution, compared with a single slit instrument. However, artifacts were observed in the reconstructed mass spectrum due to nonuniformity in the electric field and misalignment of the detector and the ion source with the mass analyzer focal plane. In this work, we modified the mass analyzer design of the previous C-CAMMS instrument to improve electric field uniformity, improve the alignment of the ion source and the mass analyzer with the detector, and increase the depth-of-focus to further facilitate alignment. A comparison of reconstructed spectra of a mixture of dry air and toluene at different electric fields was performed using the improved C-CAMMS prototype. A reduction in reconstruction artifacts compared to our proof-of-concept C-CAMMS instrument highlights the improved performance enabled by the design changes.

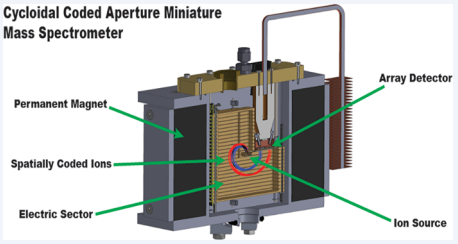

1. INTRODUCTION

Miniaturization of mass spectrometers is desirable for many applications including trace detection of explosives, pesticides, or narcotics;[1−3] point-of-care diagnostics;[4] environmental monitoring;[5−8] and space exploration.[9,10] Barriers toward miniaturization persist in the form of size, weight, and power constraints; limited detector technologies; and vacuum requirements. Additionally, miniaturization of mass spectrometers must contend with a trade-off between throughput and resolution that limits performance relative to traditional, full-scale laboratory instruments.[11] Most commonly used miniature mass spectrometers are based on ion trap, quadrupole, or time-of-flight mass analyzers.[12−14] Recently, there has been a renewed interest in miniature sector mass spectrometers due to the development of high-performance neodymium−iron−boron (Nd−Fe−B) permanent magnets that reduce the mass analyzer size and weight,[15] and ion array detectors that offer simultaneous detection of ions over a wide mass range.[16−19] Furthermore, the use of spatially coded apertures can break the trade-off between throughput and resolution in a sector mass spectrometer and increase throughput without sacrificing resolution.[11,20−23]

Spatial aperture coding is a computational sensing technique that has been historically used in optical[24,25] and X-ray imaging[26] and more recently in sector mass spectrometry.[20−23] In an analytical instrument like a sector mass spectrometer, the measurements, g, are related to the mass spectrum through the equation $g = HS + n$, where S is the input mass spectrum, n is noise, and H is the measurement matrix that incorporates the physics and architecture of the system and maps the input of the mass analyzer to the output of the mass analyzer at the detector. In a conventional sector mass spectrometer with a position-sensitive array detector, a narrow slit is used to define the position of ion input into the mass analyzer and make the measurement matrix an identity matrix.[11] This ensures that there is only one set of detector array elements (pixels) associated with each mass-to-charge (m/z), and a simple calibration of detector position (pixel number) to m/z is all that is needed to convert the detector signal to a mass spectrum. However, as the instrument size shrinks, to maintain resolution, the slit must also shrink leading to severe throughput limitations at resolutions required for most applications. In a mass analyzer incorporating computational sensing techniques, also called a computational mass spectrometer, the measurement matrix can be designed to maximize the parameters of interest like throughput and resolution. In practice, one method to achieve increased

Received: October 9, 2020
Revised: December 10, 2020
Accepted: December 11, 2020
Published: December 31, 2020

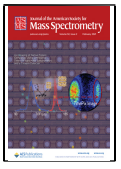

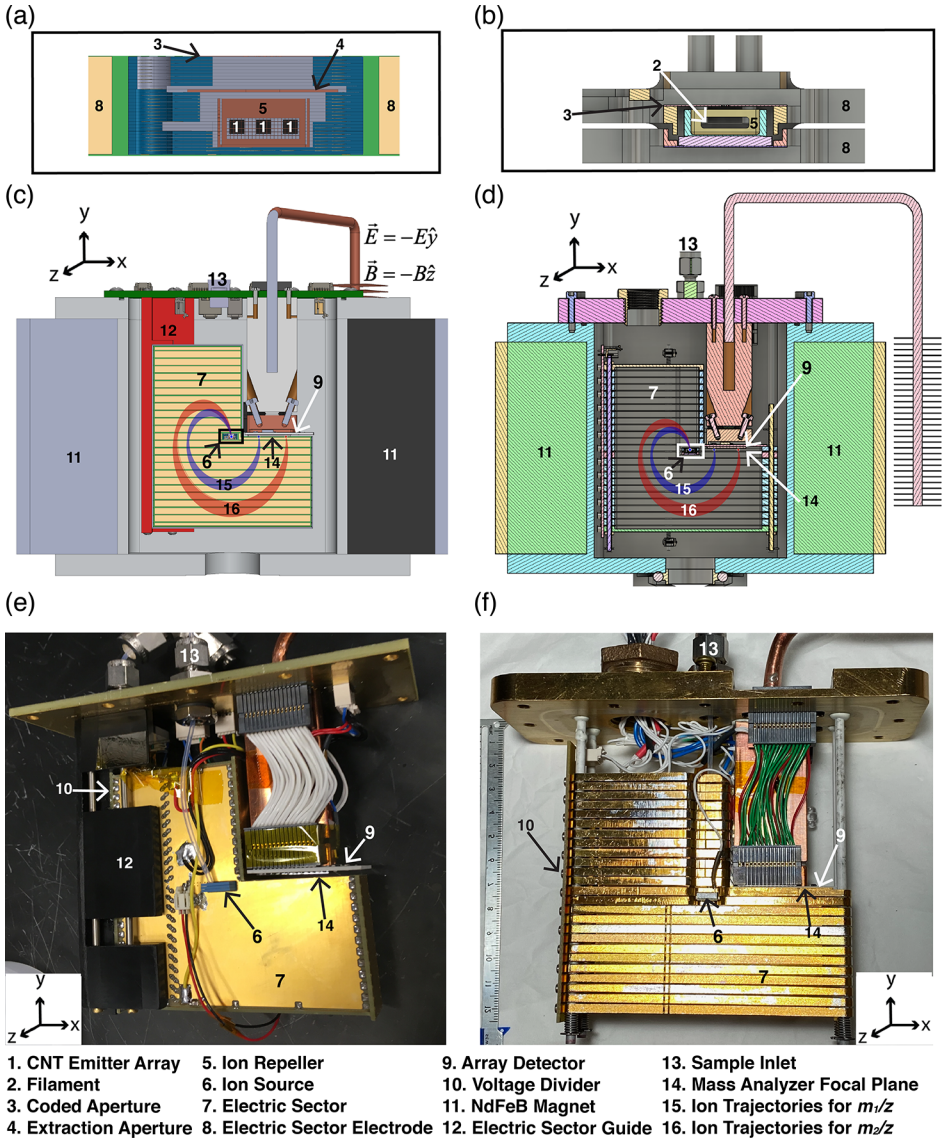

Figure 1. (a) Proof-of-concept C-CAMMS ion source CAD design cross-section, (b) new C-CAMMS-MP ion source CAD design cross-section, (c) proof-of-concept C-CAMMS CAD design cross-section containing ion trajectories for ions of two different m/z, (d) new C-CAMMS-MP CAD design cross-section containing ion trajectories for ions of two different m/z, (e) proof-of-concept C-CAMMS electric sector, ion source, and detector, and (f) new C-CAMMS-MP electric sector, ion source, and detector (magnetic sector not shown). The electric field is in the $-y$ direction, and the magnetic field is in the $-z$ direction.

throughput while maintaining resolution is by replacing a single slit with a coded aperture, or array of slits of different sizes. The total open area of the aperture's slits determines the maximum throughput while the width of the smallest slit of the aperture determines the highest resolution. The measurement matrix then contains off-diagonal elements representative of multiplexing and there is no longer a single set of detector elements for each m/z. After determination of the measurement matrix H from the physics and architecture of the system, a mass spectrum can be reconstructed from the coded spectrum for an unknown compound or compounds by solving the inverse problem $\hat{S} = H^{-1}g$, where $\hat{S}$ represents an estimate of the real spectrum S.[11]

Previous work demonstrated the ability of aperture coding to increase the throughput without sacrificing resolution in a 90° magnetic sector mass analyzer,[21,23] a Mattauch−Herzog mass analyzer,[22] and a cycloidal mass analyzer,[20] all of which were coupled with a position sensitive array detector. For the 90° and Mattauch−Herzog instruments, a distorted image of the aperture is projected on the detector that varies for each m/z due to the physics and architecture of the mass analyzer. This requires a complex construction and calibration of the measurement matrix H for spectral reconstruction. The cycloidal mass analyzer, when coupled with a focal plane array detector, is particularly well suited for use with aperture coding. The perfect focusing properties of the cycloidal mass analyzer enable a 1:1 image of the coded aperture to be projected on the detector for each m/z. Therefore, a simple deconvolution of the system response from the detector measurements is all that is required to solve the inverse problem for spectral reconstruction. The system response is estimated by deconvolving the aperture image from the spectrum of a known compound. For an isolated fragment at a single m/z, the system response is essentially equivalent to the aperture image projected on the detector at this m/z. Therefore, we try to estimate the system response using an

https://dx.doi.org/10.1021/jasms.0c00378
J. Am. Soc. Mass Spectrom. 2021, 32, 509−518

aperture image from a fragment that is spatially separated from other m/z in the spectrum. A previous proof-of-concept cycloidal coded aperture miniature mass spectrometer (C-CAMMS) employed a cycloidal mass analyzer, a carbon nanotube (CNT) field emission electron ionization source, and a capacitive transimpedance amplifier (CTIA) array detector to demonstrate an order of magnitude increase in throughput without loss in resolution, compared to a single slit instrument. However, a deconvolution of the system response from the detector measurements for spectral reconstruction resulted in artifacts in the reconstructed mass spectrum. These artifacts were caused by variations in the system response and aperture image as a function of position along the detector due to nonuniformities in the electric field and misalignment of the detector and the ion source with the mass analyzer focal plane.[20]

This paper presents a redesign of the ion source and the electric sector from the previous C-CAMMS instrument to improve the uniformity of the aperture image and system response, thereby reducing artifacts in spectral reconstruction using a simple deconvolution algorithm. The improvement in the uniformity of aperture image and system response is achieved by improving the electric field uniformity and ensuring that the detector and the ion source are better aligned with the mass analyzer focal plane. The alignment is further facilitated by reducing the angular dispersion in the ion beam caused by the ion source geometry, which increases the depth-of-focus. The improvement in consistency of the aperture image and system response results in an improvement in performance of C-CAMMS, demonstrated by generating reconstructed spectra containing a mixture of dry air and toluene with limited artifacts.

2. INSTRUMENT DESIGN

The improved C-CAMMS miniature prototype (C-CAMMS-MP) is based on the previous C-CAMMS instrument[20] and consists of a membrane inlet, a thermionic filament-based ion source, a cycloidal mass analyzer, an array detector, control electronics, and a vacuum system. The following sections describe each subsystem and the changes we made to the subcomponents in the previous C-CAMMS instrument to improve performance.

2.1. Sample Inlet and Vacuum System. The sample inlet in the previous C-CAMMS instrument was a direct-leak inlet that used a precision needle valve to control the sample flow into the C-CAMMS ion source.[20] In the new C-CAMMS-MP instrument, samples are introduced via a polydimethylsiloxane (PDMS) membrane inlet. The membrane inlet is one of the more commonly used, passive, and selective inlet techniques for mass spectrometry.[27−31] The membrane inlet in the new C-CAMMS-MP is constructed using a 1 in. long and 1/16-in. diameter hollow cylindrical PDMS membrane (Dow Corning) encased in a 1/4-in. Teflon tubing. The PDMS membrane is secured on two pieces of 1/16-in. stainless steel tubing and atmospherically sealed via a Swagelok nut and tee assembly housing Teflon ferrules. The inlet is designed such that the feed stream containing the analytes of interest permeates through the membrane and flows into the new C-CAMMS-MP vacuum, also known as a flow-through configuration.[32] The flow is then directed into the new C-CAMMS-MP ion source via a 1/16-in. diameter Teflon tube. The membrane inlet is connected to a custom gas mixing system consisting of several mass flow controllers (controlled by a LabVIEW program), pneumatic valves, and pressurized gas cylinders, as previously described.[20]

The previous C-CAMMS instrument used an Agilent Technologies IDP-15 Dry Scroll vacuum pump backing an Agilent Turbo V81 M turbo pump. In their place, the new C-CAMMS-MP employs a Pfeiffer Vacuum miniature diaphragm pump (MVP-010) and a Pfeiffer Vacuum turbomolecular pump (HiPace 10) for portability. The system base pressure is 5.3×10^{-6} mbar with the membrane inlet sealed.

2.2. Ion Source. As mentioned in the Introduction, improving the uniformity of the system response can be accomplished by increasing the depth-of-focus of the mass analyzer. Increasing the depth-of-focus reduces the precision with which the various components of the mass spectrometer need to be aligned. The depth-of-focus is increased by reducing the energy and angular dispersion of the ion beam.[20] Based on the conservation principle of ion optics, which states that the product of the spatial extent of the ion beam, the angular extents of the ion beam, and the square root of the acceleration voltage is a constant,[33,34] the ion source design must follow two key rules to generate an ion beam with low dispersion: ions must be generated over a small potential difference for low energy dispersion, and equipotential lines in the ion source must be parallel to the aperture for low angular dispersion. Figure 1a,b shows computer-aided design (CAD) cross sections of the ion sources in the previous C-CAMMS and the new C-CAMMS-MP, respectively. Figure S1 shows the positioning of the ion sources in the two instruments, and Figures S2 and S3 show additional views of the two ion sources. Figure S4 shows electron and ion trajectory simulations of the two ion sources.

The ion source in the previous C-CAMMS instrument[20] was a standalone miniature Neir-type[35] carbon nanotube (CNT) field emission electron ionization source that was inserted into a slot in the center of the electric sector.[36] It was constructed using a low-temperature cofired ceramic (LTCC) scaffold[37] containing a CNT field emitter array, an ion repeller box, an extraction aperture, and a coded aperture. The CNT emitter array was grown in an etched cavity on a silicon chip and supplied electrons for ionization. The ion repeller was constructed using an electroformed metal box with grids on opposing sides. The grids directed the transmission of electrons into the middle of the ion repeller. Positioned above the ion repeller box were extraction and coded apertures. The apertures directed ions out of the ion source and spatially filtered them.[20]

Major changes in the new C-CAMMS-MP ion source are related to ion optics, geometry, and the type of electron source used. Rather than a standalone unit like the previous ion source, the new C-CAMMS-MP ion source is incorporated into the electric sector geometry, improving alignment. The main components of the new C-CAMMS-MP ion source are a thermionic filament-based electron source, an ion repeller box, and a coded aperture. The thermionic emitter is an yttria-coated iridium filament housed in a Vespel body (Scientific Instrument Services, Inc.). The thermionic filament-based electron ionization source is more stable over time compared to the carbon nanotube-based field emission source used in the previous C-CAMMS instrument. Additionally, the width of the filament is smaller than the width of the CNT array producing a thinner sheet of electrons in the ionization volume. Therefore, the potential gradient over which ions are generated is smaller in the filament-based source, resulting in lower ion

https://dx.doi.org/10.1021/jasms.0c00378
J. Am. Soc. Mass Spectrom. 2021, 32, 509−518

energy dispersion.[38] Directly behind the filament is a gold-plated printed circuit board (PCB) used as an electron repeller to direct all the emitted electron current from the filament toward the ion repeller. The ion repeller in the new C-CAMMS-MP is machined out of titanium and plated in gold to reduce surface charge accumulation.[39,40] It is 5 mm wide, 2.4 mm wider than the one used in the previous C-CAMMS instrument. A wider ion repeller reduces angular dispersion of the ion beam by reducing curvature in the equipotential lines, making them more parallel.[38] Therefore, the new C-CAMMS-MP ion source is designed to produce a lower ion energy (27.4 ± 0.4 eV) and angular (0 ± 4°) dispersion, compared to the previous C-CAMMS ion source with a higher ion energy (26.5 ± 0.9 eV) and angular (0 ± 13°) dispersion (Figure S4). The new C-CAMMS-MP ion source does not include an extraction aperture, since our simulations indicate that it had minimal impact on ion trajectories and dispersion (Figure S4).

2.3. Vacuum Feedthrough. The new C-CAMMS-MP uses a 140 mm × 60 mm × 12.7 mm block of brass that provides an improved vacuum seal in place of the printed circuit board vacuum feedthrough used in the previous C-CAMMS instrument.[20] This new feedthrough also has 12 through-holes around the outer perimeter for 1/2 in. long 6-32 brass screws to secure it to the vacuum manifold.

2.4. Mass Analyzer. The cycloidal mass analyzer design for both the previous C-CAMMS and the new C-CAMMS-MP instruments consists of a magnetic sector constructed using a permanent magnet and an array of electrodes for the electric sector. The magnetic sector (flux density, 0.3 T) has the same opposed dipole design as described in previous publications.[20,41] Figure 1c,d shows CAD images of the electric sectors, and Figure 1e,f shows photographs of the assembled electric sectors from the previous C-CAMMS and the new C-CAMMS-MP instruments, respectively. Figures S1 and S5 show additional CAD images of the two instruments.

To generate the desired electric field, the previous C-CAMMS instrument used a PCB electric sector in the form of an L-shaped hollow box with an internal cavity 11.9 mm deep, 84.9 mm tall, and 75.9 mm wide at the base of the L and 42.4 mm wide toward the top of the L (Figure 1e). The electric sector was comprised of 25 electrodes spaced 0.5 mm apart. The top and the bottom most electrodes were 1.5 mm tall and the 23 middle electrodes were 3 mm tall. The electrodes were fabricated as gold tracks on the inner surface of a 1 mm thick 370HR (Isola) FR4 circuit board.[20] The potential on each electrode was determined by eq 1 and implemented by a power supply (Keithley 2410 source meter) series of 1 MΩ resistors arranged in a voltage divider circuit on the outer surface of the electric sector PCB.

$$V_i = \left(\frac{i - 13}{25}\right)Ed \tag{1}$$

In the above eq 1, V_i represents voltage on the ith electrode, where i = 1 for the bottom electrode in Figure 1c and varies from 1 to 25; E is the desired electric field; and d is the distance between the top and the bottom electrodes. The ion source was placed in-line with the electrically grounded electrode 13, and the detector was positioned at the edge of the L, at the mass analyzer focal plane.

There are three main issues with the previous electric sector design. First, (Figure 1e), the electric sector is attached to the electric sector guide, whereas the detector assembly is attached to the PCB feedthrough. Since the detector and the electric sectors are attached to two different scaffolds, differences in the positioning of the detector assembly in comparison with the electric sector results in misalignment of the detector with the mass analyzer. This is evident in Figure 1e, where the detector is clearly not parallel to the L of the electric sector. Second, the ion source could also be misaligned with both the detector and the mass analyzer due to the tolerance of fit between the slot and the ion source. Third, as mentioned above (and shown in Figure S3), the ion source for the previous C-CAMMS was placed in-line with the electrically grounded electrode 13. Landry et al. determined that this configuration resulted in a nonuniform electric field near the ion source.[20,41] The new C-CAMMS-MP electric sector in Figure 1f resolves the alignment issues by embedding both the ion source and the detector within its scaffolding. The following paragraphs describe the design changes to the electric sector in the new C-CAMMS-MP to fix these issues.

In the new C-CAMMS-MP (Figure 1f), the electric sector PCB from the previous C-CAMMS instrument is replaced with 3 mm thick 6061 aluminum electrodes arranged to form an electric sector retaining the L-shape with an internal cavity 15 mm deep, 84 mm tall, and 78 mm wide at the base of the L and 45.5 mm wide toward the top of the L. Each electrode is sputtered with an ∼20 nm adhesion layer of titanium, and an ∼200 nm layer of gold to reduce surface charge accumulation. The spacing between the electrodes is maintained by using 0.5 mm thick ceramic spacers. The electric sector is assembled by alternatively sliding the electrodes and ceramic spacers onto two 4-40 threaded rods and two ceramic alignment rods compressed with springs. Each electrode and spacer is designed with a tolerance of ±0.025 mm in the y-direction for a high precision sector assembly. The electric sector uses the same number of electrodes (25) and the same voltage divider eq 1 as in the previous C-CAMMS instrument. The voltages to the electrodes are applied via a series of 20 kΩ resistors arranged in a similar voltage divider circuit as the previous C-CAMMS instrument.[20] The circuit board is attached to the tall edge of the electric sector using 2-56 vented screws to make electrical contact.

As depicted in Figures S2 and S3, the ion source in the new C-CAMMS-MP is placed in a cavity between electrodes 12 and 13 in the electric sector, enabling a more homogeneous electric field surrounding the embedded ion source, as described by Landry et al.[41]

In addition, the new C-CAMMS-MP mass analyzer also resolves the detector and mass analyzer focal plane alignment issue of the previous C-CAMMS mass analyzer by creating a cavity for the detector to be placed within the electric sector electrode 13, which is electrically grounded (Figure S3). This ensures that the detector is aligned with the mass analyzer focal plane and with the ion source aperture plane. The internal width of electrode 12 immediately in front of the detector (at the mass analyzer focal plane) is reduced to 4 mm to prevent stray charge from accumulating on the ceramic carrier of the detector. Additionally, since the detector array is 3 mm wide, narrowing the internal width of the electric sector at the mass analyzer focal plane ensures that any electric fields from the detector's supporting electronics do not perturb the electric field inside the electric sector.

2.5. Detector and Control Electronics. The detector used in the new C-CAMMS-MP is the same eighth generation 1704 channel CTIA array as the one used in the previous C-CAMMS instrument.[20] Further details about the detector

https://dx.doi.org/10.1021/jasms.0c00378
J. Am. Soc. Mass Spectrom. 2021, 32, 509−518

technology are described in refs 16, 17, 20, and 42−44. A custom thermal management system is used to cool the detector and reduce thermal noise, similar to the one in the previous C-CAMMS instrument.[20] The thermal electric power was maintained at 50% duty cycle, cooling the detector to approximately −5 °C as described in ref 20.

Like the previous C-CAMMS instrument, the new C-CAMMS-MP is controlled by a combination of custom circuits, software packages, and Keithley Instruments source meters.[20] Power for the vacuum pumps, the control electronics, and the detector is supplied using a custom 24 V DC power supply. The thermal management system, the cooling system, the detector, and the vacuum pumps are managed by a custom control circuit via a Python program. The control circuit consists of a MSP430 microcontroller and several subsystem circuit modules mounted on a custom printed circuit board.[20]

3. PERFORMANCE VALIDATION AND DISCUSSION

3.1. Experimental Methods. *3.1.1. Sample Introduction Parameters.* The analyte was introduced into the membrane inlet via a custom gas mixing system consisting of several mass flow controllers and pressurized gas cylinders, as previously described.[20] Toluene (100 ppm) balanced in dry air was used as the sample analyte for validating the consistency of system response in the new C-CAMMS-MP. Analyte flow was controlled using mass flow controllers via a custom LabVIEW (NI, Austin TX) program. The new C-CAMMS-MP system pressure was maintained at 2.7×10^{-5} mbar by the membrane inlet.

3.1.2. Instrumentation Control Parameters. Voltages for the filament, the ion repeller, the electron repeller, and the electric sector were applied using Keithley 2410 source meters (Solon, OH) via a Python script. The filament was biased at a potential of −40 V relative to 30 V on the ion repeller to generate 70 eV electrons. An Agilent 3640 A power supply provides the necessary voltages for the filament. It was determined that an electron current of ∼200 nA was sufficient to generate an ion current that could cause saturation of the detector signal. Achieving 200 nA of electron emission current from the filament required a potential difference of 0.98 V across it, with 1.47 A of current running through it. The electron repeller was maintained at a voltage of −40 V to direct all the electron current from the filament toward the ion repeller. The current values on the filament, the ion repeller, and the electron repeller were measured as −200 nA, 200 nA, and 0 A, respectively, indicating that almost all of the electrons emitted by the filament reached the ion repeller. Equal and opposite voltages were applied to the top and bottom electrodes of the electric sector, with respect to the center electrode 13 that was electrically grounded. The voltage divider circuit then distributed the voltages appropriately to all the other electric sector electrodes.

To ascertain the uniformity of the system response, data was collected for various electric fields which results in ions corresponding to different mass ranges striking the detector. For instance, applying ±48 V to each end of the electric sector voltage divider results in an electric field = 1143 V/m, with ions in the mass range of m/z = 11−35 striking the detector. Applying a voltage of ±17 V results in an electric field = 405 V/m, leading to ions within a mass range of m/z = 32−100 striking the detector. The data from the detector was collected using a Python script and analyzed using custom MATLAB scripts. A deconvolution of system response from coded data/measurements to obtain reconstructed spectra was performed using the Richardson−Lucy deconvolution algorithm as it is numerically more stable than the inverse Fourier transform algorithm.[45,46]

3.2. Coded Aperture Imaging. Figure 2a shows experimental (blue) and simulated (gray) coded mass spectra of 100 ppm toluene balanced in dry air for electric field = 1143 V/m, obtained with the new C-CAMMS-MP. Figure 2b shows experimental (red) and simulated (gray) coded mass spectra of 100 ppm toluene balanced in dry air for electric field = 405 V/m obtained with the new C-CAMMS-MP. Figure 2c depicts experimental (green) and simulated (gray) coded mass spectra for 50:50 mixture of argon and dry air with the previous C-CAMMS instrument. Experimental and simulated data from detector pixels 1 to 750 in Figure 2a,c and from pixels 1 to 1100 in part b are vertically scaled by a factor of 5 for better visualization. The coded aperture used for these experiments has a pattern consisting of three slits: 100 μm, 150 μm, and 50 μm wide, separated by 100 and 150 μm, respectively. The simulated coded spectra (in gray) are constructed from NIST Chemistry WebBook data.[47] The simulated coded spectra are determined by converting the NIST data to a series of

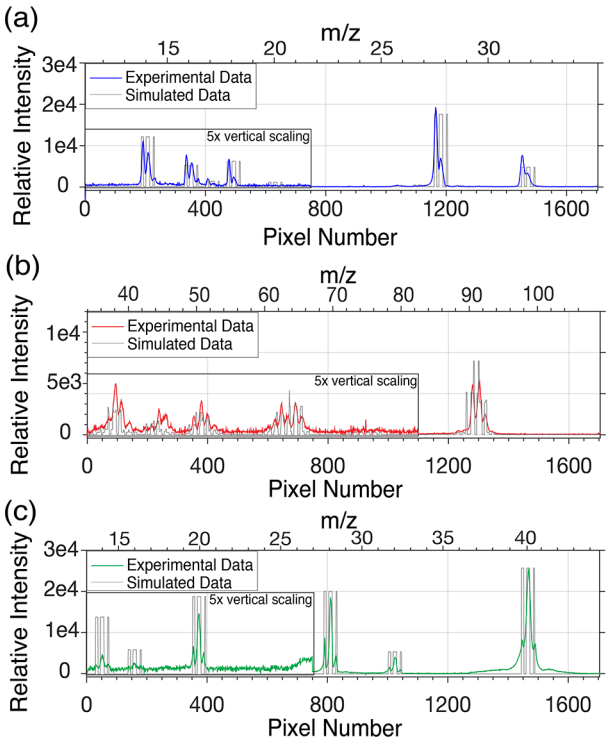

Figure 2. (a) Experimental (blue) and simulated (gray) coded mass spectra of 100 ppm toluene balanced in dry air for electric field = 1143 V/m obtained with the new C-CAMMS-MP, (b) experimental (red) and simulated (gray) coded mass spectra of 100 ppm toluene balanced in dry air for electric field = 405 V/m obtained with the new C-CAMMS-MP, (c) experimental (green) and simulated (gray) coded mass spectra for 50:50 mixture of argon and dry air with the previous C-CAMMS instrument. Experimental and simulated data from pixels 1 to 750 (as highlighted) within each of parts a and c, and from pixels 1 to 1100 (as highlighted) within part b are vertically scaled by a factor of 5 for better visualization. Also added to parts a−c are m/z axes fitted to pixel numbers to help identify ion species corresponding to each aperture image in the coded spectra.

https://dx.doi.org/10.1021/jasms.0c00378
J. Am. Soc. Mass Spectrom. 2021, 32, 509−518

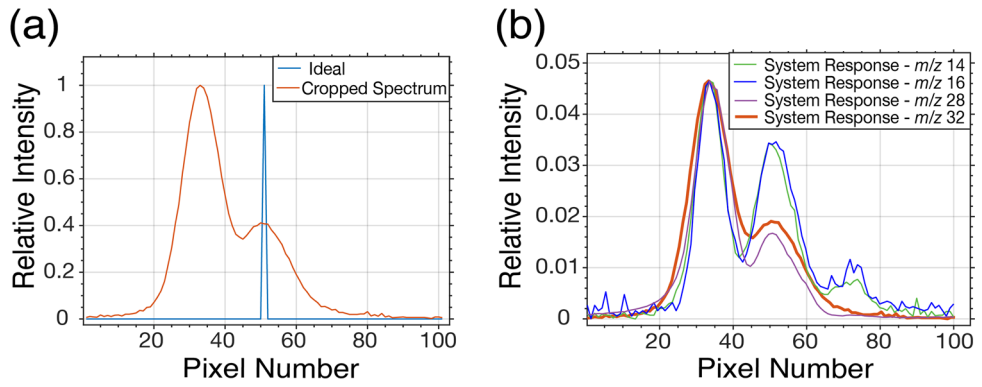

Figure 3. (a) Depiction of the cropped aperture image (for m/z = 32) and the ideal spectrum to estimate the system response/aperture image and (b) depiction of the estimated system response/aperture image for m/z = 14, 16, 28, and 32.

simulated coded aperture images corresponding to each detected ion species. The top horizontal axes in Figure 2a–c indicate the m/z corresponding to each coded aperture image. Each of the experimental and simulated coded aperture images from left to right in Figure 2a corresponds to m/z = 14, 16, 17, 18, 28, and 32, representing the ion species N^+, O^+, HO^+, H_2O^+, N_2^+, and O_2^+, respectively. Each of the experimental and simulated coded aperture images in Figure 2b corresponds to toluene ion fragments from m/z = 34 to 100. The experimental and simulated coded aperture images in Figure 2c from left to right correspond to m/z = 14, 16, 20, 28, and 32, representing N^+, O^+, Ar^{2+}, N_2^+, O_2^+, and Ar^+, respectively.

Figure 2a,b demonstrates that the experimental coded aperture images in the coded spectra do not overlap perfectly with the simulated coded aperture images, similar to our results with the previous C-CAMMS instrument. Figure 2c reproduces the data from the previous C-CAMMS instrument,[20] for a comparison with the data from the new C-CAMMS-MP in Figure 2a,b. Note that for the new C-CAMMS-MP, the data suggests that there are very few ions passing through the smallest slit, while for the previous C-CAMMS instrument, there are a significant number of ions passing through each slit. Much of the mismatch in peak intensities between the experimental aperture images for both prototypes and the simulated aperture images can be attributed to three possible factors. First, is the finite thickness of the coded aperture, the side walls of which can block some ions. Second, a nonuniform spatial distribution of ions resulting from the spatial distribution of electrons emitted from the filament could lead to fewer ions passing through the smallest slit. Finally, additional mismatches can also be attributed to variations in ion abundances caused by spatial variation on collision cross sections and dissociation rate constants.[48−50] Despite the differences in peak intensities between the experimental and simulated aperture images, their relative peak positions are in good agreement. Most importantly, reconstructed mass spectra using simple deconvolution of the system response can still be obtained without artifacts if the system response is uniform and consistent across the detector for all electric fields, as further discussed in section 3.3.

3.3. Spectral Reconstruction Process. As discussed in the Introduction, the physics of a cycloidal mass analyzer ideally results in a 1:1 image of the coded aperture on the detector. However, as shown above, variations in the spatial distribution of the ions in the ion source as well as the finite thickness of the aperture results in slight deviations of the image projected on the detector from the expected image. The coded aperture spectrum can be reconstructed into a conventional mass spectrum by following a simple three-step calibration and spectral reconstruction process.[20] First, a cropped coded aperture image $g_{O_2^+}$ from a measured coded spectrum is selected for estimating the system response. Second, the estimated system response $\hat{r}$ is obtained by deconvolving the ideal spectrum s_{NIST} from the cropped coded aperture image $g_{O_2^+}$. A caret sign above a variable represents an estimate.

$$\hat{r} = F^{-1}\left(\frac{F[g_{O_2^+}]}{F[s_{NIST}]}\right) \tag{2}$$

In eq 2, F represents a Fourier transform operation, and F^{-1} represents an inverse Fourier transform operation. Third, a deconvolution of the estimated system response $\hat{r}$ from a measured coded spectra g is performed to obtain the estimated reconstructed spectrum $\hat{s}$, as observed from eq 3, which is comparable to a conventional mass spectrum corresponding to a single-slit instrument.

$$\hat{s} = F^{-1}\left(\frac{F[g]}{F[\hat{r}]}\right) \tag{3}$$

As discussed in section 3.1 and in ref 20, the Richardson–Lucy deconvolution algorithm is used to perform deconvolution to obtain a reconstructed spectrum from eq 3.

For the purposes of this study, the aperture image corresponding to O_2^+ (m/z = 32) from Figure 2a was chosen for estimating the system response and reconstructing coded mass spectra from Figure 2a,b. The m/z = 32 aperture image was cropped to eliminate any contributions from neighboring aperture images from m/z = 31 and m/z = 33, respectively, before estimation of the system response. Figure 2c is the coded spectrum reproduced from the previous C-CAMMS instrument and, therefore, used a different system response estimation for its reconstruction, as described in ref 20. The ideal spectrum s_{NIST} is a single pixel positioned at the center of the aperture. Figure 3a depicts the cropped spectrum/aperture image for m/z = 32 from Figure 2a and its corresponding ideal spectrum to estimate the system response (Figure 3b) used in this study. Since the ideal spectrum s_{NIST} is a single pixel wide, the estimated system response $\hat{r}$ is equivalent to the aperture image $g_{O_2^+}$ (Figure 3b, red trace).

https://dx.doi.org/10.1021/jasms.0c00378
J. Am. Soc. Mass Spectrom. 2021, 32, 509−518

It is important to note that since the system response is essentially equivalent to the aperture image projected on the detector for each m/z, a constant system response will result in an artifact-free reconstructed mass spectrum acquired from eq 3. Having a constant system response makes it possible to solve the spectral reconstruction inverse problem via a simple three-step spectral reconstruction process, as described above. A nonuniform system response represents deviations in physical parameters (shape of the aperture, ion energies, applied fields) of the as-built instrument from the intended design. In that case, a complex construction and calibration of the measurement matrix H will be required for an accurate representation of the instrument and high-quality spectral reconstructions.

3.4. Reconstructed Spectra and the Consistency of System Response. Figure 4a–c depicts the results of reconstruction of the coded mass spectra from Figure 2a–c, respectively, using the estimated system response for m/z = 32 (Figure 3b). Figure 4a depicts reconstructed (blue) and ideal mass spectra (gray) of 100 ppm toluene balanced in dry air for an electric field = 1143 V/m obtained with the new C-CAMMS-MP. Figure 4b shows reconstructed (red) and ideal mass spectra (gray) of 100 ppm toluene balanced in dry air for an electric field = 405 V/m obtained with the new C-CAMMS-MP. Figure 4c depicts reconstructed (green) and ideal (gray) mass spectra for a 50:50 mixture of argon and dry air with the previous C-CAMMS instrument, for comparison. Also included in Figure 4a–c are the simulated electron ionization mass spectrum data (in gray) from NIST Chemistry WebBook.[47] Both the experimental and simulated data from pixels 1 to 750 in Figure 4a,c and from pixels 1 to 1100 in part b are vertically scaled by a factor of 5 for better visualization. Each of the reconstructed mass spectra in Figure 4a–c are calibrated for m/z on the bottom horizontal axis, with the original pixel numbers provided on the top horizontal axis. Table 1 compares the artifact height as a percentage of reconstructed peak height for the new C-CAMMS-MP at various electric fields for different m/z and with the reconstructions for the previous C-CAMMS instrument. Artifact height % represents a quantitative metric for characterizing the uniformity of system response. A low artifact height % independent of m/z, detector, and electric field is indicative of higher reconstruction quality, demonstrating a uniform system response.

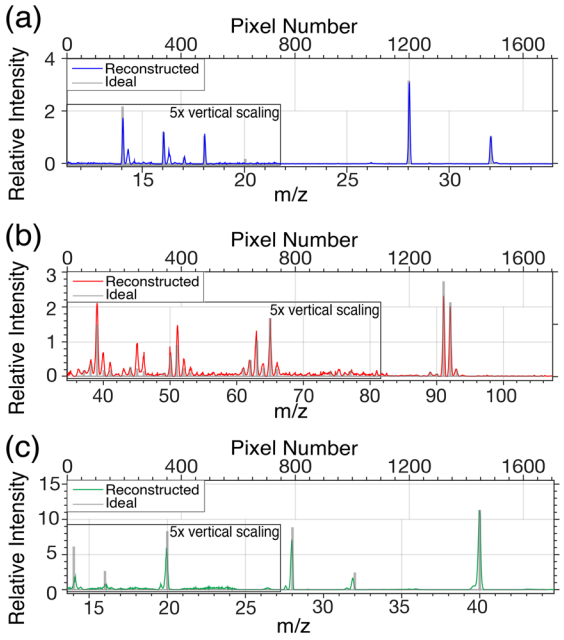

Figure 4. (a) Reconstructed (blue) and ideal mass spectra (gray) of 100 ppm toluene balanced in dry air for an electric field = 1143 V/m obtained with the new C-CAMMS-MP, (b) reconstructed (red) and ideal mass spectra (gray) of 100 ppm toluene balanced in dry air for an electric field = 405 V/m obtained with the new C-CAMMS-MP, (c) reconstructed (green) and ideal (gray) mass spectra for a 50:50 mixture of argon and dry air with the previous C-CAMMS instrument. Experimental and simulated data from pixels 1 to 750 in each of parts a and b, and from pixels 1 to 1100 in part b are vertically scaled by a factor of 5 for better visualization. Each of the reconstructed mass spectra in parts a–c are also calibrated for m/z on the bottom horizontal axis, with the original pixel numbers provided on the top horizontal axis.

Figure 4a,b and Table 1 show that the system response/aperture image is mostly uniform as a function of m/z. Only the reconstructed peaks corresponding to low m/z ion species (14, 16, 17) have significant artifacts. This is in contrast with artifacts for all the ion species present in the reconstruction for the previous C-CAMMS instrument. The presence of artifacts in the low m/z reconstruction peaks for the new C-CAMMS-MP is a result of differences in estimated system responses/aperture images for lower and higher m/z ions. Figure 3b corroborates this by demonstrating the differences in estimated system responses when using aperture images from lower (14, 16) and higher (28, 32) m/z ions.

The improved uniformity of system response for the new C-CAMMS-MP can be attributed to the improvements in instrument design that result in a uniform electric field and a better alignment of the detector and the ion source with the mass analyzer focal plane than in the previous C-CAMMS instrument. However, the reconstruction peaks corresponding to lower m/z ions have higher artifacts than expected, as a result of inconsistencies in the system response/aperture image between the lower and the higher m/z ions. Our hypothesis is that the ion species corresponding to low m/z ions illuminate the aperture differently than the higher m/z ions, causing the difference in system response between lower and higher m/z ions. Spatially nonuniform electron emission from the thermionic filament could result in a narrower ionization volume and cause ions of different m/z to illuminate the aperture differently. Figure 5 presents a schematic of the new C-CAMMS-MP ion source cross-section, depicting our hypothesis. The orthogonal electric (E_{IN}) and magnetic (flux density B) fields acting on the ion trajectories inside the ion source cause the ions to drift in the direction of the cross-product of the fields (toward the left as shown in Figure 5). The drift (d_{id}) in ion trajectories is higher for low m/z ions, as compared with the higher m/z ions, and can be estimated using eq 4.

$$d_{id} = r - \sqrt{r^2 - d_{IV\text{-}CA}{}^2} \tag{4}$$

In eq 4, $d_{IV\text{-}CA}$ is the distance between the ionization volume (where the ions are formed) and the coded aperture plane, and r is the radius of curvature of ions dispersed by a Lorentz force acting on them inside the ion source. The radius of curvature of the ions (r) can by calculated using eq 5.

$$r = \frac{1}{B}\sqrt{\frac{2mV_{IR\text{-}CA}}{q}} \tag{5}$$

https://dx.doi.org/10.1021/jasms.0c00378
J. Am. Soc. Mass Spectrom. 2021, 32, 509–518

Table 1. Comparison of the Artifact Height as a % of Reconstructed Peak Height for the New C-CAMMS-MP at Various Electric Fields and Different m/z and with the C-CAMMS Proof-of-Concept Instrument[a]

	m/z											
electric field variation	14	16	17	18	20	28	32	40	51	65	91	92
C-CAMMS proof-of-concept	20.6	35.3			9.6	6.2	6.9	5				
C-CAMMS-MP at 1143 V/m	31.4	41.7	16.4	1.8		0	5					
C-CAMMS-MP at 1023 V/m	33	30	17	1.5		0	0					
C-CAMMS-MP at 881 V/m		42.6	8.6	2		0	0					
C-CAMMS-MP at 761 V/m				0		0.6	1.5	0				
C-CAMMS-MP at 619 V/m						1.3	0.7	0				
C-CAMMS-MP at 428 V/m							0	0	0	0	0	0
C-CAMMS-MP at 404 V/m								0	0	0	0	0

[a]Empty cells in the table represent no data obtained due to absence of reconstruction peaks corresponding to that m/z.

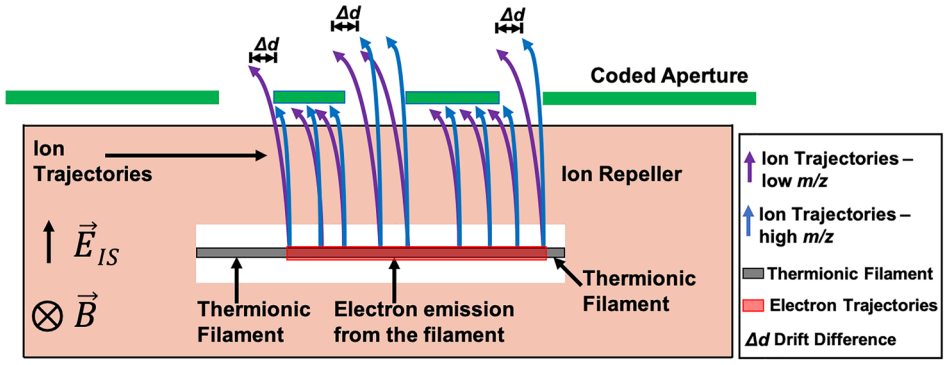

Figure 5. Demonstration of the hypothesis that the coded aperture could be illuminated as a function of m/z. An ionic drift in the direction of $E_{IN} \times B$ could result in an illumination of the coded aperture as a function of m/z, aided by a narrower ionization volume caused by nonuniform electron emission from the thermionic filament. The difference in ionic drift is highlighted by Δd in the figure. The trajectories corresponding to higher m/z ions (in blue) only illuminate the rightmost two slits of the coded aperture, whereas the trajectories corresponding to lower m/z ions (in purple), with a higher ionic drift, illuminate all three slits of the coded aperture.

In eq 5, m is the mass of an ion, q is the charge of an ion, B is the magnetic flux density, and $V_{IR\text{-}CA}$ is the potential difference between the ion repeller and the coded aperture. Using $d_{IV\text{-}CA} = 1.15$ mm, $m = (1.67 \times 10^{-27}) \times 28$ kg for N_2^+ ions and $m = (1.67 \times 10^{-27}) \times 14$ kg for N^+ ions, $q = (1.6 \times 10^{-19})$ C, $B = 0.297$ T, $V_{IR\text{-}CA} = 30$ V, we obtain $d_{id} = 47$ μm for the higher m/z N_2^+ ions and $d_{id} = 67$ μm for the lower m/z N^+ ions.

Figure 5 demonstrates how a nonuniform electron emission from the thermionic filament could result in a narrower ionization volume that could further impact the ionic drift, resulting in an illumination of the coded aperture as a function of m/z. The trajectories corresponding to higher m/z ions (in blue) only illuminate the rightmost two slits of the coded aperture, whereas the trajectories corresponding to lower m/z ions (in purple) with a higher ionic drift illuminate all three slits of the coded aperture. It is important to note that the ionic thermal velocities are much lower in magnitude compared to ionic drift velocities and, therefore, are unlikely to impact the ionic drift. A redesign of the ion source to reduce its height would also reduce the effects of ionic drift in the direction of the cross-product of the fields. Alternatively, using a more complex reconstruction process as described in refs 21 and 23, where the full measurement matrix is generated instead of using the simple deconvolution described here, would remove the artifacts at low m/z in the reconstruction. The full measurement matrix can incorporate variations in the system response as a function of position and m/z and will be investigated in future publications.

4. CONCLUSION

This paper demonstrated a miniature cycloidal coded aperture mass spectrometer, with improvements in instrument design over the proof-of-concept C-CAMMS previously described by Amsden et al.[20] We have shown that it is possible to obtain a more uniform system response in a miniature cycloidal mass analyzer, with drastically reduced reconstruction artifacts, by improving the electric field uniformity, the alignment between ion source/detector and mass analyzer focal plane, and by reducing dispersion caused by the ion source to further improve alignment. Some artifacts in the reconstruction peaks corresponding to lower m/z ions still persist, due to differences in the system response/aperture image between the lower and higher m/z ions, possibly caused by a nonuniform illumination of the aperture as a function of the m/z. This variation in aperture illumination is likely a result of the drift in ion trajectories, aided by a narrower ionization volume caused by a spatially nonuniform electron emission from the thermionic filament. Future C-CAMMS based instruments will focus on changing the ion source geometry to limit the effects of ion drift and development of a more complex reconstruction algorithm to account for nonuniformities in the system response.

■ ASSOCIATED CONTENT

Supporting Information

The Supporting Information is available free of charge at https://pubs.acs.org/doi/10.1021/jasms.0c00378.

https://dx.doi.org/10.1021/jasms.0c00378
J. Am. Soc. Mass Spectrom. 2021, 32, 509−518

3-D CAD models of the new C-CAMMS-MP and the previous C-CAMMS mass analyzers; 3-D CAD models of the ion source and detector assembly within the electric sector electrodes; cross-section of the CAD models for the new C-CAMMS-MP and the previous C-CAMMS ion sources and the detector and their relative positioning within the electric sector electrodes; electron and ion trajectories corresponding to the previous C-CAMMS ion source and the new C-CAMMS-MP ion source; and cross-section of the CAD models for the previous C-CAMMS and the new C-CAMMS-MP mass analyzers (PDF)

AUTHOR INFORMATION

Corresponding Author

Jason J. Amsden − *Department of Electrical and Computer Engineering, Duke University, Durham, North Carolina 27708, United States;* orcid.org/0000-0002-3900-192X; Phone: (919)660-5592; Email: jason.amsden@duke.edu

Authors

Raul Vyas − *Department of Electrical and Computer Engineering, Duke University, Durham, North Carolina 27708, United States*

Tanouir Aloui − *Department of Electrical and Computer Engineering, Duke University, Durham, North Carolina 27708, United States*

Kathleen Horvath − *Department of Electrical and Computer Engineering, Duke University, Durham, North Carolina 27708, United States*

Philip J. Herr − *Department of Electrical and Computer Engineering, Duke University, Durham, North Carolina 27708, United States*

Matthew P. Kirley − *Department of Electrical and Computer Engineering, Duke University, Durham, North Carolina 27708, United States;* orcid.org/0000-0002-6124-1575

Charles B. Parker − *Department of Electrical and Computer Engineering, Duke University, Durham, North Carolina 27708, United States*

Adam D. Keil − *Broadway Analytical, LLC, Monmouth, Illinois 61462, United States*

James B. Carlson − *Engineering and Applied Physics Division, RTI International, Research Triangle Park, North Carolina 27709, United States*

Justin Keogh − *Department of Chemistry and Biochemistry, University of Arizona, Tucson, Arizona 85721, United States*

Roger P. Sperline − *Department of Chemistry and Biochemistry, University of Arizona, Tucson, Arizona 85721, United States*

M. Bonner Denton − *Department of Chemistry and Biochemistry, University of Arizona, Tucson, Arizona 85721, United States*

M. Luisa Sartorelli − *Department of Electrical and Computer Engineering, Duke University, Durham, North Carolina 27708, United States; Departamento de Física, Universidade Federal de Santa Catarina, 88040-000 Florianópolis, Santa Catarina, Brazil*

Brian R. Stoner − *Department of Electrical and Computer Engineering, Duke University, Durham, North Carolina 27708, United States*

Michael E. Gehm − *Department of Electrical and Computer Engineering, Duke University, Durham, North Carolina 27708, United States;* orcid.org/0000-0003-4163-749X

Jeffrey T. Glass − *Department of Electrical and Computer Engineering, Duke University, Durham, North Carolina 27708, United States*

Complete contact information is available at: https://pubs.acs.org/10.1021/jasms.0c00378

Notes

The authors declare no competing financial interest.

ACKNOWLEDGMENTS

The information, data, and work presented herein was funded in part by the Advanced Research Projects Agency-Energy (ARPA-E), U.S. Department of Energy, under Award Number DE-AR0000546. The views and opinions of authors expressed herein do not necessarily state or reflect those of the United States Government or any agency thereof.

REFERENCES

(1) Sanders, N. L.; Kothari, S.; Huang, G.; Salazar, G.; Cooks, R. G. Detection of Explosives as Negative Ions Directly from Surfaces Using a Miniature Mass Spectrometer. *Anal. Chem.* **2010**, *82*, 5313−5316.

(2) Chen, C.-H.; Lin, Z.; Tian, R.; Shi, R.; Cooks, R. G.; Ouyang, Z. Real-time sample analysis using a sampling probe and miniature mass spectrometer. *Anal. Chem.* **2015**, *87*, 8867−8873.

(3) Hendricks, P. I.; Dalgleish, J. K.; Shelley, J. T.; Kirleis, M. A.; McNicholas, M. T.; Li, L.; Chen, T.-C.; Chen, C.-H.; Duncan, J. S.; Boudreau, F.; Noll, R. J.; Denton, J. P.; Roach, T. A.; Ouyang, Z.; Cooks, R. G. Autonomous in situ analysis and real-time chemical detection using a backpack miniature mass spectrometer: concept, instrumentation development, and performance. *Anal. Chem.* **2014**, *86*, 2900−2908.

(4) Kirby, A. E.; Lafrenière, N. M.; Seale, B.; Hendricks, P. I.; Cooks, R. G.; Wheeler, A. R. Analysis on the go: quantitation of drugs of abuse in dried urine with digital microfluidics and miniature mass spectrometry. *Anal. Chem.* **2014**, *86*, 6121−6129.

(5) Camilli, R.; Reddy, C. M.; Yoerger, D. R.; Van Mooy, B. A.; Jakuba, M. V.; Kinsey, J. C.; McIntyre, C. P.; Sylva, S. P.; Maloney, J. V. Tracking hydrocarbon plume transport and biodegradation at Deepwater Horizon. *Science* **2010**, *330*, 201−204.

(6) Keil, A.; Hernandez-Soto, H.; Noll, R. J.; Fico, M.; Gao, L.; Ouyang, Z.; Cooks, R. G. Monitoring of toxic compounds in air using a handheld rectilinear ion trap mass spectrometer. *Anal. Chem.* **2008**, *80*, 734−741.

(7) Mach, P. M.; Winfield, J. L.; Aguilar, R. A.; Wright, K. C.; Verbeck, G. F. A portable mass spectrometer study targeting anthropogenic contaminants in Sub-Antarctic Puerto Williams, Chile. *Int. J. Mass Spectrom.* **2017**, *422*, 148−153.

(8) Bell, R. J.; Davey, N. G.; Martinsen, M.; Collin-Hansen, C.; Krogh, E. T.; Gill, C. G. A field-portable membrane introduction mass spectrometer for real-time quantitation and spatial mapping of atmospheric and aqueous contaminants. *J. Am. Soc. Mass Spectrom.* **2015**, *26*, 212−223.

(9) Arevalo, R.; Ni, Z.; Danell, R. M. Mass spectrometry and planetary exploration: A brief review and future projection. *J. Mass Spectrom.* **2020**, *55*, e4454.

(10) Ren, Z.; Guo, M.; Cheng, Y.; Wang, Y.; Sun, W.; Zhang, H.; Dong, M.; Li, G. A review of the development and application of space miniature mass spectrometers. *Vacuum* **2018**, *155*, 108−117.

(11) Amsden, J. J.; Gehm, M. E.; Russell, Z. E.; Chen, E. X.; Di Dona, S. T.; Wolter, S. D.; Danell, R. M.; Kibelka, G.; Parker, C. B.; Stoner, B. R.; Brady, D. J.; Glass, J. T. Coded apertures in mass spectrometry. *Annu. Rev. Anal. Chem.* **2017**, *10*, 141−156.

(12) Badman, E. R.; Graham Cooks, R. Miniature mass analyzers. *J. Mass Spectrom.* **2000**, *35*, 659−671.

(13) Ouyang, Z.; Cooks, R. G. Miniature Mass Spectrometers. *Annu. Rev. Anal. Chem.* **2009**, *2*, 187−214.

(14) Maher, S.; Jjunju, F. P.; Taylor, S. Colloquium: 100 years of mass spectrometry: Perspectives and future trends. *Rev. Mod. Phys.* **2015**, *87* (113), 113.
(15) Herbst, J.; Croat, J. Neodymium-iron-boron permanent magnets. *J. Magn. Magn. Mater.* **1991**, *100*, 57−78.
(16) Felton, J. A.; Schilling, G. D.; Ray, S. J.; Sperline, R. P.; Denton, M. B.; Barinaga, C. J.; Koppenaal, D. W.; Hieftje, G. M. Evaluation of a fourth-generation focal plane camera for use in plasma-source mass spectrometry. *J. Anal. At. Spectrom.* **2011**, *26*, 300−304.
(17) Barnes; Schilling, G. D.; Sperline, R.; Denton, M. B.; Young, E. T.; Barinaga, C. J.; Koppenaal, D. W.; Hieftje, G. M. Characterization of a focal plane camera fitted to a Mattauch−Herzog geometry mass spectrograph. 2. Use with an inductively coupled plasma. *Anal. Chem.* **2004**, *76*, 2531−2536.
(18) Sinha, M. P.; Wadsworth, M. Miniature focal plane mass spectrometer with 1000-pixel modified-CCD detector array for direct ion measurement. *Rev. Sci. Instrum.* **2005**, *76*, 025103.
(19) Hadjar, O.; Johnson, G.; Laskin, J.; Kibelka, G.; Shill, S.; Kuhn, K.; Cameron, C.; Kassan, S. IonCCD for direct position-sensitive charged-particle detection: from electrons and keV ions to hyperthermal biomolecular ions. *J. Am. Soc. Mass Spectrom.* **2011**, *22*, 612−623.
(20) Amsden, J. J.; Herr, P. J.; Landry, D. M. W.; Kim, W.; Vyas, R.; Parker, C. B.; Kirley, M. P.; Keil, A. D.; Gilchrist, K. H.; Radauscher, E. J.; Hall, S. D.; Carlson, J. B.; Baldasaro, N.; Stokes, D.; Di Dona, S. T.; Russell, Z. E.; Grego, S.; Edwards, S. J.; Sperline, R. P.; Denton, M. B.; Stoner, B. R.; Gehm, M. E.; Glass, J. T. Proof of concept coded aperture miniature mass spectrometer using a cycloidal sector mass analyzer, a carbon nanotube (CNT) field emission electron ionization source, and an array detector. *J. Am. Soc. Mass Spectrom.* **2018**, *29*, 360−372.
(21) Chen, E. X.; Russell, Z. E.; Amsden, J. J.; Wolter, S. D.; Danell, R. M.; Parker, C. B.; Stoner, B. R.; Gehm, M. E.; Glass, J. T.; Brady, D. J. Order of magnitude signal gain in magnetic sector mass spectrometry via aperture coding. *J. Am. Soc. Mass Spectrom.* **2015**, *26*, 1633−1640.
(22) Russell, Z. E.; DiDona, S. T.; Amsden, J. J.; Parker, C. B.; Kibelka, G.; Gehm, M. E.; Glass, J. T. Compatibility of spatially coded apertures with a miniature Mattauch-Herzog mass spectrograph. *J. Am. Soc. Mass Spectrom.* **2016**, *27*, 578−584.
(23) Russell, Z. E.; Chen, E. X.; Amsden, J. J.; Wolter, S. D.; Danell, R. M.; Parker, C. B.; Stoner, B. R.; Gehm, M. E.; Brady, D. J.; Glass, J. T. Two-dimensional aperture coding for magnetic sector mass spectrometry. *J. Am. Soc. Mass Spectrom.* **2015**, *26*, 248−256.
(24) Brady, D. J. *Optical Imaging and Spectroscopy*; John Wiley & Sons, 2009.
(25) Wagadarikar, A. A.; Gehm, M. E.; Brady, D. J. Performance comparison of aperture codes for multimodal, multiplex spectroscopy. *Appl. Opt.* **2007**, *46*, 4932−4942.
(26) MacCabe, K.; Krishnamurthy, K.; Chawla, A.; Marks, D.; Samei, E.; Brady, D. Pencil beam coded aperture x-ray scatter imaging. *Opt. Express* **2012**, *20*, 16310−16320.
(27) Bier, M.; Kotiaho, T.; Cooks, R. Direct insertion membrane probe for selective introduction of organic compounds into a mass spectrometer. *Anal. Chim. Acta* **1990**, *231*, 175−190.
(28) Ketola, R. A.; Kotiaho, T.; Cisper, M. E.; Allen, T. M. Environmental applications of membrane introduction mass spectrometry. *J. Mass Spectrom.* **2002**, *37*, 457−476.
(29) Kotiaho, T. On-site environmental and in situ process analysis by mass spectrometry. *J. Mass Spectrom.* **1996**, *31*, 1−15.
(30) Lauritsen, F. R.; Kotiaho, T. Advances in membrane inlet mass spectrometry (MIMS). *Rev. Anal. Chem.* **1996**, *15*, 237−264.
(31) Virkki, V. T.; Ketola, R. A.; Ojala, M.; Kotiaho, T.; Komppa, V.; Grove, A.; Facchetti, S. On-Site Environmental Analysis by Membrane Inlet Mass Spectrometry. *Anal. Chem.* **1995**, *67*, 1421−1425.
(32) LaPack, M. A.; Tou, J. C.; Enke, C. G. Membrane mass spectrometry for the direct trace analysis of volatile organic compounds in air and water. *Anal. Chem.* **1990**, *62*, 1265−1271.
(33) Ioanoviciu, D. Ion Optics. In *Aspects of Charged Particle Optics*; Advances in Electronics and Electron Physics, Vol. 73; Hawkes, P. W., Ed.; Academic Press, 1989; pp 1−92, DOI: 10.1016/S0065-2539(08)60567-3.
(34) Brunnée, C. The ideal mass analyzer: Fact or fiction? *Int. J. Mass Spectrom. Ion Processes* **1987**, *76*, 125−237.
(35) Nier, A. O. A Mass Spectrometer for Routine Isotope Abundance Measurements. *Rev. Sci. Instrum.* **1940**, *11*, 212−216.
(36) Saito, Y.; Uemura, S. Field emission from carbon nanotubes and its application to electron sources. *Carbon* **2000**, *38*, 169−182.
(37) Radauscher, E. J.; Parker, C. B.; Gilchrist, K. H.; Di Dona, S.; Russell, Z. E.; Hall, S. D.; Carlson, J. B.; Grego, S.; Edwards, S. J.; Sperline, R. P.; Denton, M. B.; Stoner, B. R.; Glass, J. T.; Amsden, J. J. A miniature electron ionization source fabricated using micro-electromechanical systems (MEMS) with integrated carbon nanotube (CNT) field emission cathodes and low-temperature co-fired ceramics (LTCC). *Int. J. Mass Spectrom.* **2017**, *422*, 162−169.
(38) Vyas, R.; Herr, P. J.; Aloui, T.; Horvath, K.; Kirley, M. P.; Parker, C. B.; Keil, A. D.; Carlson, J. B.; Keogh, J.; Sperline, R. P.; Denton, M. B.; Sartorelli, M. L.; Stoner, B. R.; Gehm, M. E.; Glass, J. T.; Amsden, J. J. Comparison of thermionic filament and carbon nanotube field emitter-based electron ionization sources in cycloidal coded aperture mass analyzers. *Int. J. Mass Spectrom.* **2020**, *457*, 116415.
(39) D'Autry, W.; Wolfs, K.; Yarramraju, S.; Schepdael, A. V.; Hoogmartens, J.; Adams, E. Characterization and improvement of signal drift associated with electron ionization quadrupole mass spectrometry. *Anal. Chem.* **2010**, *82*, 6480−6486.
(40) Toombs, P.; Bennett, P. Electrical Resistance of Thin Triode-Sputtered Gold Films. *J. Appl. Phys.* **1968**, *39*, 2948−2953.
(41) Landry, D. M.; Kim, W.; Amsden, J. J.; Di Dona, S. T.; Choi, H.; Haley, L.; Russell, Z. E.; Parker, C. B.; Glass, J. T.; Gehm, M. E. Effects of magnetic and electric field uniformity on coded aperture imaging quality in a cycloidal mass analyzer. *J. Am. Soc. Mass Spectrom.* **2018**, *29*, 352−359.
(42) Barnes; Sperline, R.; Denton, M. B.; Barinaga, C. J.; Koppenaal, D.; Young, E. T.; Hieftje, G. M. Characterization of a focal plane camera fitted to a Mattauch−Herzog geometry mass spectrograph. 1. Use with a glow-discharge source. *Anal. Chem.* **2002**, *74*, 5327−5332.
(43) Schilling, G. D.; Andrade, F. J.; Barnes; Sperline, R. P.; Denton, M. B.; Barinaga, C. J.; Koppenaal, D. W.; Hieftje, G. M. Characterization of a Second-Generation Focal-Plane Camera Coupled to an Inductively Coupled Plasma Mattauch−Herzog Geometry Mass Spectrograph. *Anal. Chem.* **2006**, *78*, 4319−4325.
(44) Schilling, G. D.; Ray, S. J.; Rubinshtein, A. A.; Felton, J. A.; Sperline, R. P.; Denton, M. B.; Barinaga, C. J.; Koppenaal, D. W.; Hieftje, G. M. Evaluation of a 512-Channel Faraday-Strip Array Detector Coupled to an Inductively Coupled Plasma Mattauch−Herzog Mass Spectrograph. *Anal. Chem.* **2009**, *81*, 5467−5473.
(45) Lucy, L. B. An iterative technique for the rectification of observed distributions. *Astron. J.* **1974**, *79*, 745.
(46) Richardson, W. H. Bayesian-Based Iterative Method of Image Restoration. *J. Opt. Soc. Am.* **1972**, *62*, 55−59.
(47) Linstrom, P. J.; Mallard, W. G. The NIST Chemistry WebBook: A chemical data resource on the internet. *J. Chem. Eng. Data* **2001**, *46*, 1059−1063.
(48) Margolin Eren, K. J.; Elkabets, O.; Amirav, A. A comparison of electron ionization mass spectra obtained at 70 eV, low electron energies, and with cold EI and their NIST library identification probabilities. *J. Mass Spectrom.* **2020**, *55*, e4646.
(49) Maccoll, A. Low-Energy, low-temperature mass spectra. 14—A simple model for the rate coefficient. *Org. Mass Spectrom.* **1991**, *26*, 235−240.
(50) Chupka, W. Effect of thermal energy on ionization efficiency curves of fragment ions. *J. Chem. Phys.* **1971**, *54*, 1936−1947.

https://dx.doi.org/10.1021/jasms.0c00378
J. Am. Soc. Mass Spectrom. 2021, 32, 509−518